Inorganic Chemistry

ARTICLE

pubs.acs.org/IC

End-to-End Azide-Bridged Manganese(III) Chain Compounds: Field-Induced Magnetic Phase Transitions and Variation of T_C to 38 K Depending on the Side Groups of the Schiff Bases

Jung Hee Yoon,[†] Woo Ram Lee,[†] Dae Won Ryu,[†] Jin Wuk Lee,[†] Sung Won Yoon,[‡] Byoung Jin Suh,[‡] Hyoung Chan Kim,[§] and Chang Seop Hong*[,†]

[†]Department of Chemistry, Research Institute for Natural Sciences, Korea University, Seoul 136-713, Korea

[‡]Department of Physics, The Catholic University of Korea, Buchon 420-743, Korea

[§]National Fusion Research Institute, Daejeon 305-333, Korea

Supporting Information

ABSTRACT: Three one-dimensional coordination polymers $[Mn(L)(N_3)]_n$ [L = L1 (**1**), L2 (**2**), L3 (**3**); $L1H_2$ = *N*,*N*′-bis(5-chlorosalicylideneiminato)-1, 3-diaminopentane, $L2H_2$ = *N*,*N*′-bis(5-bromosalicylideneiminato)-1, 3-diaminopentane, $L3H_2$ = *N*,*N*′-bis(5-bromosalicylideneiminato)-1, 3-diamino-2-dimethylpropane] bridged by end-to-end azides were prepared. The crystal systems differ according to the Schiff bases used. Each Mn atom adopts a typical Jahn−Teller distortion. The helicity of the chains occurs in a racemic manner only for **2**. No noncovalent forces are relevant in **2**, while $\pi-\pi$ contacts are visible in **1** and **3**. Magnetic measurements show the presence of apparent spin canting. Complexes **1** and **3** exhibit a field-induced metamagnetic transition from an antiferromagnetic state to a weak ferromagnetic phase, whereas **2** embraces a field-induced two-step magnetic phase transition. The critical temperature is observed at 38 K for **2**, which is relatively higher than those for **1** (11 K) and **3** (10 K). The pronounced long-range order may contribute from intrachain exchange couplings and through-space dipolar interactions between adjacent chains.

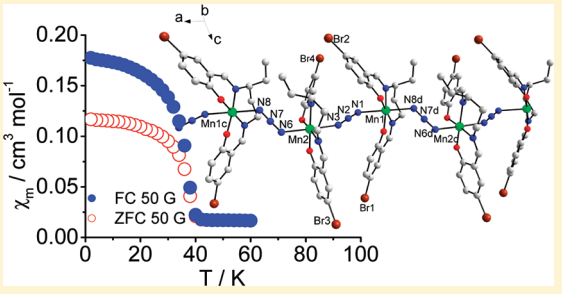

INTRODUCTION

Molecule-based magnetic materials have been actively studied for their potential applications in magnetic devices, and considerable progress has been made in the pursuit of constructing anisotropic low-dimensional molecular nanomagnets with magnetization relaxations and high-dimensional coordination networks with long-range magnetic ordering. The former concerns the development of single-molecule magnets (SMMs)[1−5] and single-chain magnets (SCMs)[6−8] that require single-ion anisotropy and negligible intermolecular or interchain magnetic interactions. Under these conditions, the characteristic slow relaxation of magnetization emerges in anisotropic molecular systems. For the latter, it is generally believed that spin centers should interact magnetically in a three-dimensional (3D) manner to bring about long-range magnetic alignment.

To achieve the aforementioned molecular magnetic systems with exotic properties, it is essential to select appropriate bridging ligands that can hold paramagnetic centers closely together and communicate effective magnetic exchange coupling between them. In this line, it is desirable to use ligands with short paths such as oxide, cyanide, carboxylate, or azide and so on.[9−12] Among them, azide acts as a bridge in diverse binding modes, for instance, μ-1,1-N_3 (or single end-on), di-μ-1,1-N_3 (double end-on), μ-1,3-N_3 (single end-to-end), di-μ-1,3-N_3 (double end-to-end), μ-1,1,1-N_3, μ-1,1,3-N_3, μ-1,1,1,1-N_3, μ-1,1,3,3-N_3, and μ-1,1,1,3,3,3-N_3.[13]

From a magnetic point of view, end-on azide generally provides ferromagnetic interaction and end-to-end azide facilitates antiferromagnetic coupling, although there are several exceptional cases.[14−16] Many structures with the azide ligand have been examined using paramagnetic transition-metal ions (Mn^{2+}, Mn^{3+}, Fe^{2+}, Co^{2+}, Ni^{2+}, Cu^{2+}, etc.),[17−23] and the magnetic properties relying on the metal contents were revealed. Among them, the Co^{2+} ion shows strong magnetic anisotropy to give intriguing magnetic characteristics of spin canting, metamagnetism, slow magnetic relaxation, and long-range order.[18,24−28] Similarly, the Mn^{III} ion, whose oxidation state is stabilized in the N_2O_2 environment of tetradentate Schiff bases, allows for significant magnetic anisotropy in association with typical Jahn−Teller distortion.[29] The use of the Schiff bases in an equatorial coordination makes two axial sites available for incoming azide ligands. Accordingly, the self-assembly of the Mn^{III} Schiff bases with azide led to the formation of dinuclear entities and frequently constrained one-dimensional (1D) chains.[30−38] The SMM behavior was observed in some discrete molecules,[30,39] and a few Mn^{III} chain systems bridged by a single azide exhibited spin canting and slow relaxation dynamics coupled with field-induced magnetic transitions and/or antiferromagnetic order.[36,37]

Received: June 20, 2011
Published: October 06, 2011

ACS Publications © 2011 American Chemical Society

On the other hand, despite such 1D Mn^{III} structures, the bulk properties of the critical temperature and coercive field have been demonstrated, as low as $T < 11$ K and as large as $H = 2.3$ kG, respectively, as a result of the degree of interchain interaction and the effect of magnetic anisotropy.[30−38] In molecular magnets, it is important to know the factors affecting the critical temperature and coercive field for the sake of the fundamental understanding of long-range order and practical application issues. It is thus highly sought to establish a simple anisotropic system, and in this regard, we have been interested in investigating such azide-linked Mn^{III} chains chelated with various tetradentate Schiff bases.

Herein we report the syntheses, crystal structures, and magnetic properties of three 1D chains, $[Mn(L)(N_3)]_n$ [L = L1 (**1**), L2 (**2**), L3 (**3**); $L1H_2$ = *N*,*N*′-bis(5-chlorosalicylideneiminato)-1,3-diaminopentane, $L2H_2$ = *N*,*N*′-bis(5-bromosalicylideneiminato)-1,3-diaminopentane, $L3H_2$ = *N*,*N*′-bis(5-bromosalicylideneiminato)-1,3-diamino-2-dimethylpropane], linked by end-to-end azides. Antiferromagnetic interactions between Mn^{III} spins within a chain are operating through the azide bridges, and spin canting clearly arises at low temperatures. Field-induced magnetic transitions are realized in the 1D chain systems. It is noted that a long-range order occurs at a high temperature of 38 K for **2** devoid of any noncovalent interaction between chains, which may be due to the extensive incorporation of dipolar interactions across the lattice. A low critical temperature is seen at 11 K for **1** and at 10 K for **3**, where interchain $\pi-\pi$ contacts are involved. Compound **3** has a relatively high coercive field of 2.8 kG.

EXPERIMENTAL SECTION

To synthesize **1**, an aqueous solution of 10 mL of NaN_3 (7 mg, 0.10 mmol) was added to a methanol solution (30 mL) of $[Mn(L1)(H_2O)]\cdot ClO_4$ (48 mg, 0.10 mmol). After stirring for several minutes, the mixture was filtered. After a few days, brown crystals were obtained. The crystals were filtered off, washed with methanol, and dried in air. Yield: 42%. Anal. Calcd for $C_{19}H_{18}Cl_2MnN_5O_2$: C, 48.12; H, 3.83; N, 14.77. Found: C, 48.33; H, 3.79; N, 14.46. IR (KBr): ν_{N_3} 2056(sh), 2040(vs), 1983(w). Complexes **2** and **3** were prepared by the same procedure as that of **1** using $[Mn(L2)(H_2O)]\cdot ClO_4$ for **2** or $[Mn(L3)(H_2O)]\cdot ClO_4$ for **3** instead of $[Mn(L1)(H_2O)]\cdot ClO_4$. Yield of **2**: 30%. Anal. Calcd for $C_{38}H_{36}Br_4Mn_2N_{10}O_4$: C, 40.52; H, 3.22; N, 12.44. Found: C, 40.42; H, 3.27; N, 12.23. IR (KBr): ν_{N_3} 2046(vs), 1990(sh). Yield of **3**: 39%. Anal. Calcd for $C_{19}H_{18}Br_2MnN_5O_2$: C, 40.52; H, 3.22; N, 12.44. Found: C, 40.55; H, 3.24; N, 11.95. IR (KBr): ν_{N_3} 2052(vs), 1983(w). The purity of the bulk samples was verified by powder X-ray diffraction (PXRD; see Figure S1 in the Supporting Information).

Physical Measurements. Elemental analyses for C, H, and N were performed at the Elemental Analysis Service Center of Sogang University. IR spectra were obtained from KBr pellets with a Bomen MB-104 spectrometer. PXRD data were recorded using Cu Kα (λ = 1.5406 Å) on a Rigaku Ultima III diffractometer with a scan speed of 3° min^{-1} and a step size of 0.01°. Magnetic susceptibilities for **1**−**3** in eicosane were carried out using a Quantum Design SQUID susceptometer (direct current, dc) and a PPMS magnetometer (alternating current, ac). Corrections for the sample holder and eicosane were made, and diamagnetic corrections of all samples were estimated from Pascal's Tables.

Crystallographic Structure Determination. X-ray data for **1**−**3** were collected on a Bruker SMART APEXII diffractometer equipped with graphite-monochromated Mo Kα radiation (λ = 0.71073 Å). A preliminary orientation matrix and cell parameters were determined from three sets of ω scans at different starting angles. Data frames were obtained at scan intervals of 0.5° with an exposure time of 10 s $frame^{-1}$. The reflection data were corrected for Lorentz and polarization factors.

Table 1. Crystallographic Data for 1 - 3

	1	2	3
formula	$C_{19}H_{18}Cl_2MnN_5O_2$	$C_{38}H_{36}Br_4Mn_2N_{10}O_4$	$C_{19}H_{18}Br_2MnN_5O_2$
M_r	474.22	1126.29	563.14
T (K)	293	100	298
cryst syst	orthorhombic	triclinic	monoclinic
space group	*Pbca*	$P\bar{1}$	$P2_1/c$
a (Å)	29.3009(17)	11.8425(10)	12.6256(15)
b (Å)	11.3200(6)	12.7124(10)	12.8577(16)
c (Å)	12.0634(7)	15.4367(16)	12.4425(15)
α (deg)	90	97.999(4)	90
β (deg)	90	112.472(3)	90
γ (deg)	90	96.399(3)	90
V (Å^3)	4001.3(4)	2091.9(3)	2019.9(4)
Z	8	2	4
ρ_{calc} (g cm^{-3})	1.574	1.788	1.852
μ (mm^{-1})	0.953	4.477	4.636
F(000)	1936	1112	1112
total no. of reflns	60 355	33 430	15 490
GOF	1.029	0.994	0.885
R1[a] [$I \geq 2\sigma(I)$]	0.0541	0.0764	0.0533
wR2[b] [$I \geq 2\sigma(I)$]	0.1256	0.1558	0.0681

[a] $R1 = \Sigma||F_o| - |F_c||/\Sigma|F_c|$. [b] $wR2 = [\Sigma w(F_o^2 - F_c^2)^2/\Sigma w(F_o^2)^2]^{1/2}$.

Absorption corrections were carried out using *SADABS*. The structures were solved by direct methods and refined by full-matrix least-squares analysis using anisotropic thermal parameters for non-H atoms with the *SHELXTL* program. All H atoms for **1**−**3** were calculated at idealized positions and refined with the riding models. For **3**, we performed *ADDSYM*, an algorithm for missing symmetry on *WingX*, to check the space group, and no obvious space group change was suggested. Crystallographic data for **1**−**3** are summarized in Table 1.

RESULTS AND DISCUSSION

Description of the Structures. The structures of **1**−**3** have been characterized using single-crystal X-ray diffraction techniques.

Complexes 1 and 2. Complex **1** crystallizes in the orthorhombic system (*Pbca*), whereas **2** belongs to the triclinic ($P\bar{1}$) system. The crystal structures of **1** and **2** and their extended two-dimensional (2D) arrays are illustrated in Figures 1 and 2. The structure of **1** is not identical with that of **2**. This suggests that the change in the halides (Cl for **1** and Br for **2**) on the 5 position of the Schiff bases is responsible for such discernible influence on the crystal system and structure. Each Mn center consists of a distorted octahedron surrounded by two N atoms from the bridging azides and N_2O_2 donors from the corresponding tetradentate Schiff bases (L1 and L2). For **1**, the Mn−N_{ax} (ax = axial) distances are long, 2.317(4) Å for Mn1−N1 and 2.252(4) Å for Mn1−N3b (b, x, 0.5 − y, 0.5 + z). Comparatively, the average Mn−$N(O)_{eq}$ (eq = equatorial) length in the equatorial N_2O_2 plane of L1 corresponds to 1.96(7) Å. The typical tetragonal elongation thus points out the presence of a Jahn−Teller distortion, as is found in many octahedral high-spin Mn^{III} entities.[29−38] In the case of **2**, the Jahn−Teller effect also occurs as judged by the long apical Mn−N_{ax} lengths [2.297(8) Å for Mn1−N1, 2.249(9) Å for Mn1−N8d (d, −1 + x, y, z), 2.260(8) Å for Mn2−N3, and 2.240(9) Å for Mn2−N6] and the short average Mn−$N(O)_{eq}$

dx.doi.org/10.1021/ic2013232 |*Inorg. Chem.* 2011, 50, 10777–10785

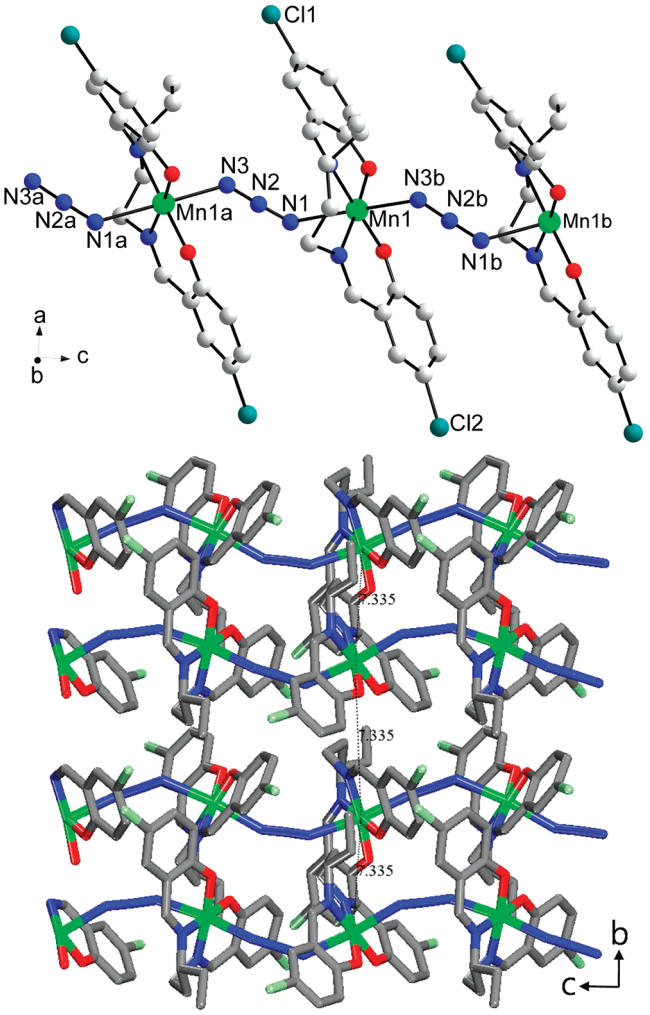

Figure 1. Top: Molecular view of **1** with the atom-labeling schemes. Symmetry codes: a, x, 0.5 − y, −0.5 + z; b, x, 0.5 − y, 0.5 + z. Bottom: Extended 2D view showing the shortest interchain distance (dotted lines).

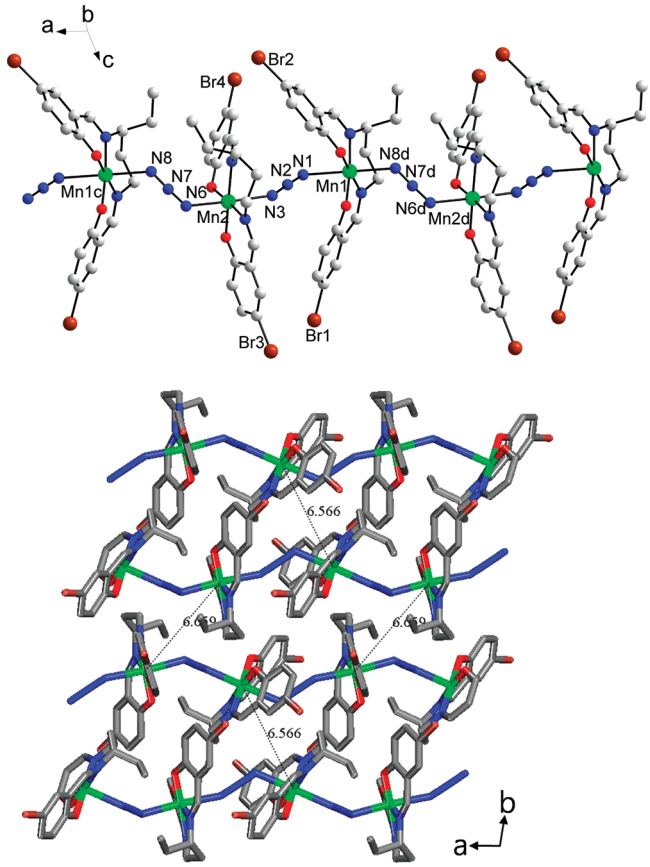

Figure 2. Top: Crystal structure of **2** showing the atom-labeling schemes. Symmetry codes: c, 1 + x, y, z; d, −1 + x, y, z. Bottom: Extended 2D view with the shortest interchain distance (dotted lines).

distance of 1.97(8) Å. The Mn−N_{ax}−N_{ax} angles in the bridging pathways are 125.6(3)° for Mn1−N1−N2 and 133.9(4)° for Mn1−N3b−N2b (**1**) and 119.1(6)° for Mn1−N1−N2, 129.9(8)° for Mn1−N8d−N7d, 149.6(7)° for Mn2−N3−N2, and 122.5(8)° for Mn2−N6−N7 (**2**). Notice that the average Mn−N_{ax} length (2.285 Å) of **1** is longer than that (2.268 Å) of **2**, while the mean Mn−N_{ax}−N_{ax} angle (129.8°) of **1** is similar to that (130.3°) of **2**. The torsion angles of Mn−N_{ax}---N_{ax}−Mn are 116.0° for **1** and 131.1° and 159.3° for **2**. The azide ligand connects two adjacent Mn^{III} ions in an end-to-end mode with Mn−Mn distances of 6.069 Å for Mn1−Mn1a (**1**; a, x, 0.5 − y, −0.5 + z) and 6.250 Å for Mn1−Mn2 and 6.009 Å for Mn2−Mn1c (**2**; c, 1 + x, y, z) to generate a 1D linear-chain structure.

In the extended structure of **1** with the Cl-substituted Schiff base L1 (Figures 1 and S2 in the Supporting Information), chains are running along the c axis. The chains are separated with the shortest Mn−Mn distance of 7.335 Å. The tiny $\pi-\pi$ interactions with a centroid distance of 3.955 Å are established between the phenoxide rings of L1, and the interchain Mn−Mn distance via the contacts is equal to 11.204 Å (Figure S3 in the Supporting Information). When Cl atoms are replaced with Br, the overall crystal packing is subject to severe changes, as shown in Figures 2 and S4 in the Supporting Information. The noticeable structural alteration in **2**, compared with **1**, is that the shortest interchain Mn−Mn distances are reduced to 6.566 and 6.659 Å, although another Mn−Mn distance between the other chains slightly increases to 11.633 Å. Interestingly, *P*- and *M*-helical chains with a long pitch length of 11.843 Å in the lattice of **2** are efficiently packed together in a heterochiral fashion, eventually resulting in a racemate (Figure S5 in the Supporting Information). This racemic arrangement was often encountered in systems composed of not only archiral but also chiral ligands.[40,41]

Complex 3. The use of L3 with the dimethyl-substituted propylene linker and 5-positioned Br groups affords the end-to-end azide-bridged 1D chain system crystallized in the monoclinic system with the space group $P2_1/c$ (Figure 3). This material exhibits an analogous octahedral environment around a Mn^{III} center in which the Mn−N_{ax} lengths are 2.269(4) Å for Mn1−N1 and 2.289(4) Å for Mn1−N3e (e, x, 1.5 − y, 0.5 + z) and the average Mn−$N(O)_{eq}$ length is 1.96(7) Å. The Mn−N_{ax}−N_{ax} angles are 137.9(3)° for Mn1−N1−N2 and 128.3(3)° for Mn1−N3e−N2e. The mean Mn−N_{ax} length (2.279 Å) lies between **1** and **2**, while the average Mn−N_{ax}−N_{ax} angle (133.1°) is larger than that of **1** and **2**. The torsion angle of Mn−N_{ax}---N_{ax}−Mn along the chain corresponds to 128.6°, and the intrachain distance through the azide bridge is 6.231 Å. In the extended structure of **3** (Figures 3 and S6 and S7 in the Supporting Information), weak $\pi-\pi$ stacking exists between the phenoxide rings with a centroid distance of 3.742 Å and the

dx.doi.org/10.1021/ic2013232 |*Inorg. Chem.* 2011, 50, 10777–10785

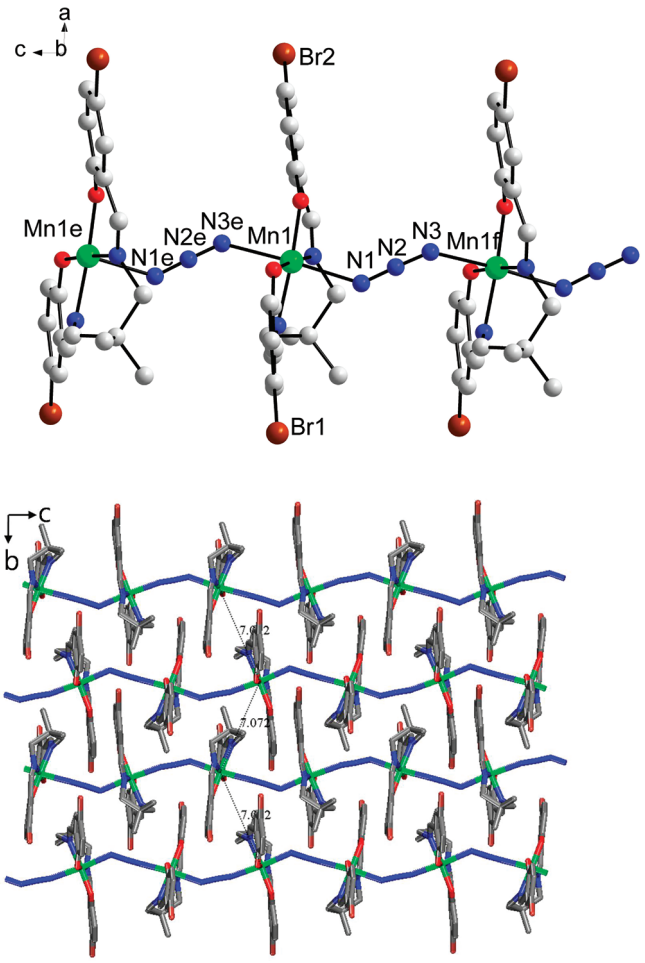

Figure 3. Top: Crystal structure of **3** showing the atom-labeling schemes. Symmetry codes: e, *x*, 1.5 − *y*, 0.5 + *z*; f, *x*, 1.5 − *y*, −0.5 + *z*. Bottom: Extended 2D view with the shortest interchain distance (dotted lines).

shortest interchain Mn−Mn distance via the noncovalent force is 7.072 Å. The other interchain Mn−Mn distance along the *c* axis is 12.626 Å.

Magnetic Properties of 1 and 2. The thermal variations in the dc magnetic susceptibility data of **1** and **2** were collected at $H = 1$ kG and $T = 2-300$ K (Figure 4). The $\chi_m T$ values at 300 K are 2.87 and 2.52 $cm^3\ K\ mol^{-1}$ for **1** and **2**, respectively, which are somewhat smaller than the spin-only one expected for a noncoupled Mn^{III} ($S_{Mn} = 2$) ion. The $\chi_m T$ product declines as the temperature is lowered and a minimum arrives at 15 K for **1** and at 40 K for **2**. Below these temperatures, a cusp becomes visible, followed by a further decay of $\chi_m T$ down to 2 K. The upturn in $\chi_m T$ at low temperatures is due to the occurrence of spin canting in the antiferromagnetic system arising from the involvement of single-ion anisotropy of a Mn^{III} ion and two types of Mn^{III} ions along the chain direction. These factors energetically favor the perpendicular orientation for the coupled spins induced by the antisymmetric Dzyaloshinsky−Moriya (D−M) coupling, resulting in spin canting.[42,43] Similar spin-canted phenomena were also revealed in several cobalt(II), nickel(II), and manganese(III) complexes bridged by diverse bridging ligands.[44−46] The interchain antiferromagnetic interactions and zero-field splitting of the complexes may account for the final decrease in the $\chi_m T(T)$ plots below the cusp temperatures.

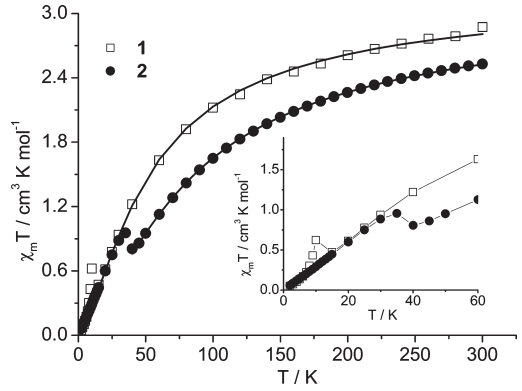

Figure 4. Plots of $\chi_m T$ versus T for **1** and **2** at 1000 G. The solid lines in the main panel show the best magnetic fits.

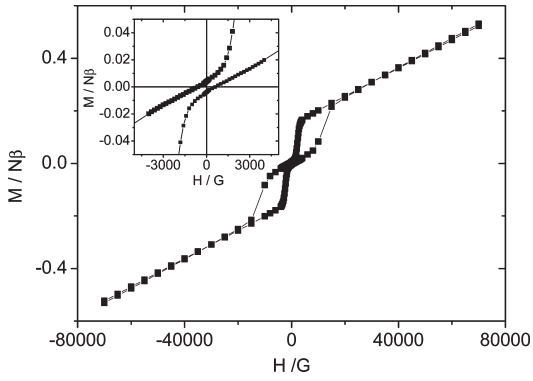

Figure 5. Plot of M versus H for **1** at 2 K. The inset is a blowup of the low-field magnetization data.

To probe the magnetic exchange coupling constants within a chain, we employed an infinite-chain model derived by Fisher ($H = -J\Sigma_i S_{A_i} \cdot S_{A_{i+1}}$) in the high-temperature range to preclude the interchain magnetic contributions and zero-field-splitting effects.[47] The fitting process gives the best-fit parameters of $g = 2.07(1)$ and $J = -7.3(1)$ cm^{-1} for **1** at $T > 15$ K and $g = 2.05(1)$ and $J = -11.5(1)$ cm^{-1} for **2** at $T > 40$ K. The negative J values indicate the existence of intrachain antiferromagntic coupling between the Mn spins mediated by end-to-end azides, and the coupling strength falls into the usual range of end-to-end azide-bridged Mn^{III} systems.[29]

To examine the magnetic nature of **1**, we measured the field-dependent magnetization data at several temperatures (Figures 5 and S8 in the Supporting Information). The magnetization amounts to 0.53 Nβ in a field of 7 T, which is not saturated and is away from the theoretical value of 4 Nβ assuming $g = 2$. The coercive field (H_{cr}) at 2 K is 600 G. An extrapolation of the high-field straight section of the magnetization to zero field approaches 0.15 Nβ and the canting angle, based on $\sin^{-1}(M_w/M_s)$, where M_s is the saturation magnetization and M_W a magnetization induced by a weak magnetic field, is 2.2° at 2 K. In the derivative of M against H at 2 K (Figure S9 in the Supporting Information), a positive peak is shown at $H_C = \sim 10$ kG. As the temperature varies, H_C tends to lessen (~7 kG at 3 K, ~6 kG at 4 and 5 K, and ~5.5 kG at 7 and 9 K) and eventually vanish at $T = 11$ K. To gain in-depth insight into the magnetic feature, the field-cooled (FC) magnetizations were collected in the field range from 20 G to 25 kG (Figure 6). An abrupt rise in the $\chi_m(T)$

dx.doi.org/10.1021/ic2013232 |*Inorg. Chem.* 2011, 50, 10777–10785

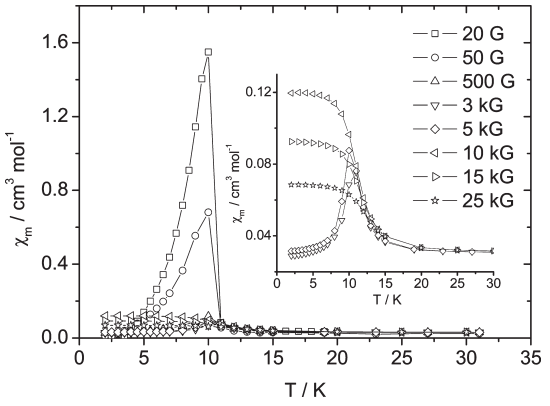

Figure 6. Plots of FC data versus T for **1** at the different magnetic fields.

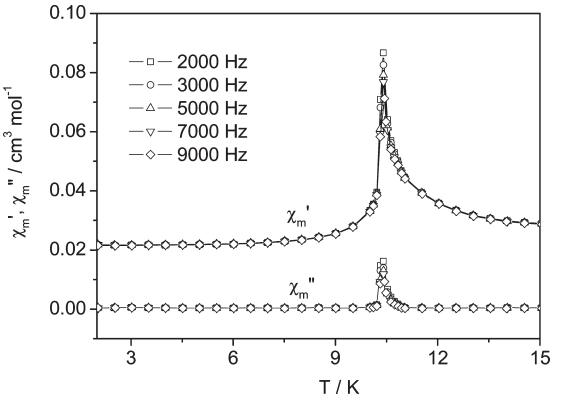

Figure 7. In-phase (χ_m') and out-of-phase (χ_m'') components for **1** with increasing frequencies.

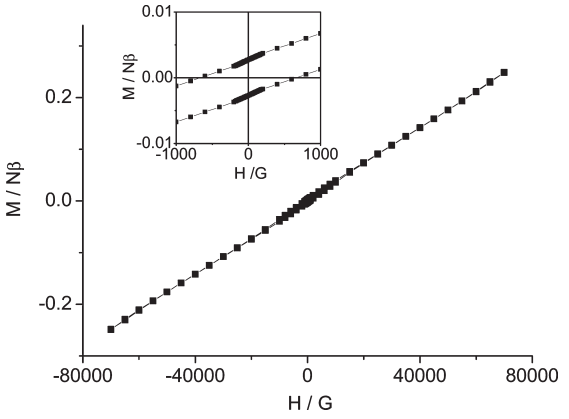

Figure 8. Plot of M versus H for **2** at 2 K. The inset is a blowup of the low-field magnetization data.

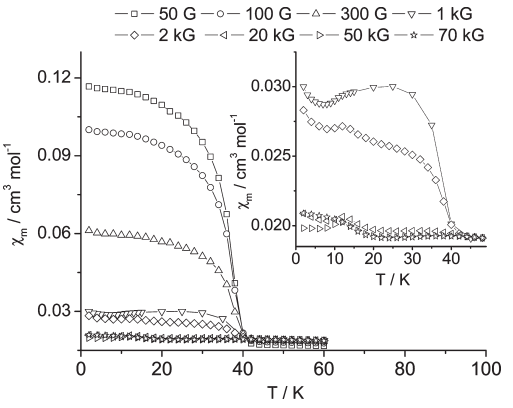

Figure 9. Plots of FC data versus T for **2** at the different magnetic fields.

curve begins at ~11 K in the low-field regime and then lowering the temperature causes χ_m to be significantly reduced. The maximum peak at ~10 K survives until H = 5 kG and disappears at $H \geq$ 10 kG. This behavior is typical of a field-induced metamagnetic transition from an antiferromagnetic state to a spin-canted phase (the weak ferromagnetic phase). Stabilization of the antiferromagnetic state seems to be in connection with the existence of the $\pi-\pi$-stacking interactions. The observed $M(H)$ and $M(T)$ data demonstrate that the weak interchain interactions between canted-spin chains are overcome by an external magnetic field of $H > H_C$, leading to a weak ferromagnetic phase. The $H-T$ phase diagram is plotted in Figure S10 in the Supporting Information.

The FC and zero-field-cooled (ZFC) magnetizations were recorded at 50 G, and there is thermomagnetic irreversibility starting from T_c = 11 K determined by the FC dM/dH curve (Figure S11 in the Supporting Information). This divergence of FC and ZFC may be related to superparamagnets, spin glasses, or magnetic domain movements. To elucidate the genuine character, ac magnetic susceptibility data were collected at zero dc field, an ac field of 5 G, and various oscillating frequencies (Figure 7). Because no frequency dependence is detectable, the possibility of superparamagnets and spin glasses can be discarded. Consequently, the irreversible response in the FC/ZFC curves supports the presence of a magnetized phase, as ascertained by the hysteresis behavior in the $M(H)$ data. From the ac plot, the in-phase (χ_m') and out-of-phase (χ_m'') signals are located at T_c = 11 K, implying the onset of long-range magnetic ordering.

The field dependence of the magnetization for **2** is displayed in Figure 8. The magnetization data slowly increase with the field, suggesting the operation of dominant antiferromagnetic interactions. The magnetization value of 0.25 Nβ at 70 kG is much smaller than that of **1**. The coercive field (H_{cr}) of 650 G in **2** is analogous to that in **1**. The extrapolated remnant magnetization at H = 0 G is 0.0035 Nβ, and the canting angle is calculated to be 0.05°. The inflection point in the $M(H)$ plot shows that a field-induced two-step transition occurs at critical fields of H_1 = 8 kG and H_2 = 60 kG (Figure S12 in the Supporting Information). The first critical field may be ascribed to a transition from a spin-canted state to another spin-canted (spin-flop) phase, and the second may be a spin reorientation to the field direction. It is estimated that the anisotropy (H_A) and exchange fields (H_E) are 1.1 and 31 kG, respectively. The H_A/H_E ratio is 3.5 × 10^{-2}, which is slightly larger than those of $S = {}^5/_2$ Heisenberg antiferromagnets with a spin-flop transition.[48] Similar properties were also observed in some anisotropic manganese(III) and cobalt(II) complexes.[49−51] To inspect the magnetic trait in detail, the FC magnetizations were recorded at diverse magnetic fields, as illustrated in Figure 9. No peaks are observed in the FC plots in the low-field range, which is contrary to **1**, where the sharp maxima are placed at low temperatures and fields. This behavior indicates the presence of a weak ferromagnetic state in the FC process at those fields. An obvious transition evolves at 38 K in the low-field region, and the χ_m response is inclined to decrease with increasing field and is almost suppressed at $H \geq$ 20 kG.

dx.doi.org/10.1021/ic2013232 |Inorg. Chem. 2011, 50, 10777–10785

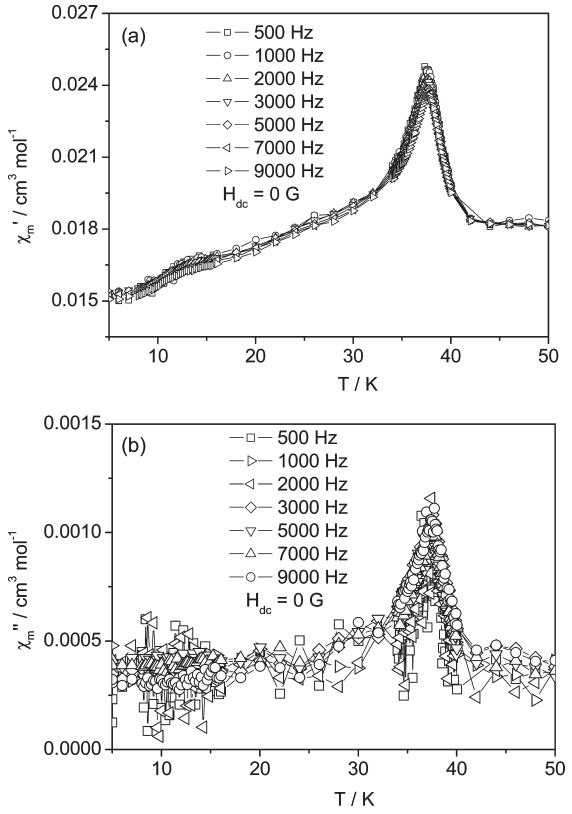

Figure 10. (a) In-phase (χ_m') and (b) out-of-phase (χ_m'') components for **2** with increasing frequencies.

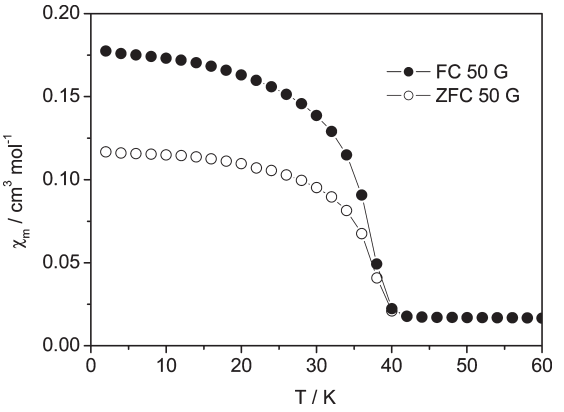

Figure 11. Temperature dependence of FC and ZFC for **2** at 50 G.

Interestingly, a hump is evident at 12 K, which disappears at H = 70 kG. This is tentatively assigned to antiferromagnetic ordering throughout the 3D lattice because χ_m' signals are present but rough χ_m'' responses appear to be absent in the same temperature range (Figure 10). The $H-T$ phase diagram is suggested in Figure S13 in the Supporting Information.

The FC and ZFC curves of **2** are depicted in Figure 11. The saturated behavior at low temperatures denotes the existence of weak ferromagnetism in FC and ZFC. They are split below T_c = 38 K, which is determined by the inflection point in the $M(T)$ data. This can be attributed to the formation of magnetic domains. Under the FC process, the domain walls move freely and the size of the domains grows. In the ZFC process, the domains are randomly oriented and frozen. The application of a magnetic field is not sufficient to unlock the domain wall motions, giving the observed $M_{ZFC} < M_{FC}$. In the ac magnetic data (Figure 10), the critical temperature is confirmed at T_c = 38 K, where a sharp peak in χ_m' and χ_m'' coincides. The apex in χ_m'' pertains to the beginning of a ferromagnetically ordered state. The peak position is independent of the oscillating frequency, suggesting that there are no glassy or superparamagnetic behavior. It is noted that, as far as the 1D chain structure is concerned, the T_c of 38 K in **2** is relatively high and is even greater than that of 2D cobalt(II) azide multilayer systems with T_c = 23 K at best.[27]

Theoretically, it is impossible to obtain a magnetized phase in a 1D chain. However, when interchain magnetic interactions turn out to be sizable in a real system, a 1D compound can give rise to long-range magnetic order. From the structural data of **2**, it is apparent that the chains in the *bc* plane are most closely positioned among all of the complexes (Figure 2). It is conjectured that the chains are magnetically correlated to some extent to realize a 2D magnetic array. The combined 2D layers may be further coupled through space, albeit weakly. Such an extended correlation may create long-range order when anisotropic Mn^{III} ions are incorporated in the chains. To check this scenario, we scrutinized the critical temperature region $(1 - T/T_c < 10^{-2}-10^{-1})$.[52] The thermodynamic behavior of the spontaneous magnetization can be expressed by the asymptotic power law $M = M_0(1 - T/T_c)^{\beta}$, where M_0 is the critical amplitude and β is the critical exponent.[53] The β term is related to the spin and lattice dimensionality. In the double-logarithmic plot of M versus the reduced temperature (Figure S14 in the Supporting Information), a linear fit of the data to the equation with T_c = 38 K yields β = 0.21. The β value remains between theoretical 2D Ising (β = 0.125) and 3D Ising (β = 0.325) arrays or 3D Heisenberg (β = 0.364) magnetic systems.[52] Provided there are no noncovalent interchain contacts in **2**, the long-range order could not result from quantum exchange interactions, which can be transmitted by noncovalent hydrogen bonds or $\pi-\pi$-stacking forces. The superexchange interaction, if any, is also known to rapidly fade away with increasing interchain spacing so that it seldom explains the observed high critical temperature.[54] The other possibility is a through-space dipolar interaction, as exemplified in copper(II) hybrid inorganic–organic layered compounds, where T_c was observed at ~20 K with an interlayer spacing as large as 40 Å.[54−56] Accordingly, the critical analysis (β = 0.21) of **2** supports that a 2D spin lattice is formed by dipolar interactions through the shortest spacings (6.613 Å on average) between the nearest neighboring chains (bottom of Figure 2) and each quasi-2D magnetic layer is weakly interacted through the other type of dipolar interaction via the longer spacing (11.633 Å), eventually promoting 3D magnetic ordering.

When it comes to the critical feature of **2**, it is worth mentioning that T_c surprisingly enhances by 27 K with a change of Cl in L1 (**1**) to Br in L2 (**2**). In 2D layered magnets, in-plane exchange coupling ($J_{in\text{-}plane}$) imposes a substantial impact on T_c, while variation of the interplanar spacing ($j_{interplane}$) slightly affects T_c. The relationship of T_c with J and j can be expressed as $T_c = 4\pi J_{in\text{-}plane}/\ln(J_{in\text{-}plane}/j_{interplane})$.[54] On the basis of this expression, the noteworthy T_c in **2** may be primarily associated with the enhanced magnetic correlation in the quasi-2D lattices, the stronger intrachain magnetic coupling (J) of **2** than of **1**, as well as the closer interchain distance in the *ab* plane of **2** than in the *bc* plane of **1**.

Magnetic Properties of 3. The thermomagnetic data of **3** were collected at 1 kG and at temperatures in the range from 2

dx.doi.org/10.1021/ic2013232 |*Inorg. Chem.* 2011, 50, 10777–10785

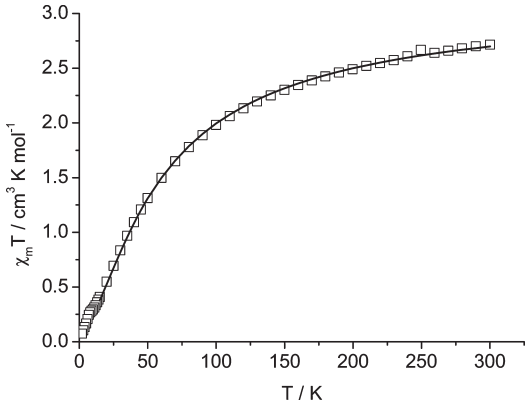

Figure 12. Plot of $\chi_m T$ versus T for **3** at 1000 G. The solid line presents the best magnetic fit.

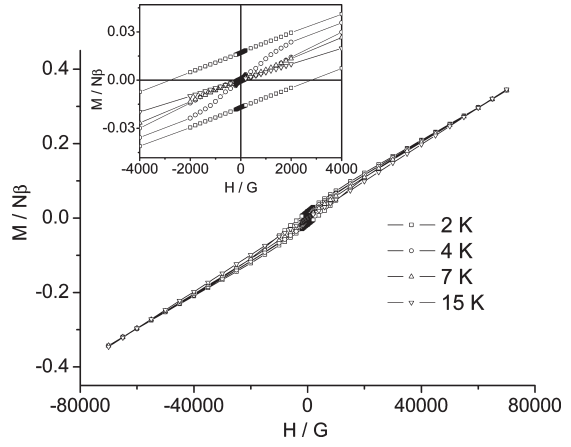

Figure 13. Plots of M versus H for **3** at several fields. The inset is a blowup of the low-field magnetization data.

to 300 K, as shown in Figure 12. The $\chi_m T$ value of 2.72 cm^3 K mol^{-1} at 300 K, which is similar to those of **1** and **2**, decreases steadily with cooling of the sample and reaches a shoulder at $T \approx 9$ K. Below that temperature, $\chi_m T$ decreases again. The overall reduction in $\chi_m T$ is a signature of the antiferromagnetic interactions. The occurrence of a shoulder can be ascribed to the canted phenomenon of neighboring spins. The intrachain magnetic exchange interaction can be assayed using the Fisher chain model.[47] A best fit affords $g = 2.05(1)$ and $J = -8.0(1)$ cm^{-1} at $T > 15$ K, and the J magnitude is similar to that of **1** but smaller than that of **2**. The order of magnetic strength appears to be paralleled by the average Mn−N_{ax} bond length.

Isothermal magnetization of **3** was measured in the field range of -70 kG $\leq H \leq 70$ kG at several temperatures (Figure 13). The magnetization increases slowly and reaches 0.34 Nβ at 70 kG, which is much smaller than saturation. This feature shows the involvement of the antiferromagnetic interactions and magnetic anisotropy of the material. The linear part of the high-field region is taken to compute a canting angle of 0.49°. In the hysteresis loop, H_{cr} at 2 K is 2.8 kG, which is the highest value of the azide-bridged Mn^{III} systems.[29] H_{cr} decreases to 120 G at 4 K and 10 G at 7 K. In the azide-bridged cobalt(II) layered compounds, the coercive field tends to decrease with increasing interlayer spacing because of weakening of the anisotropy field.[27] In addition, intralayer structures together with other factors

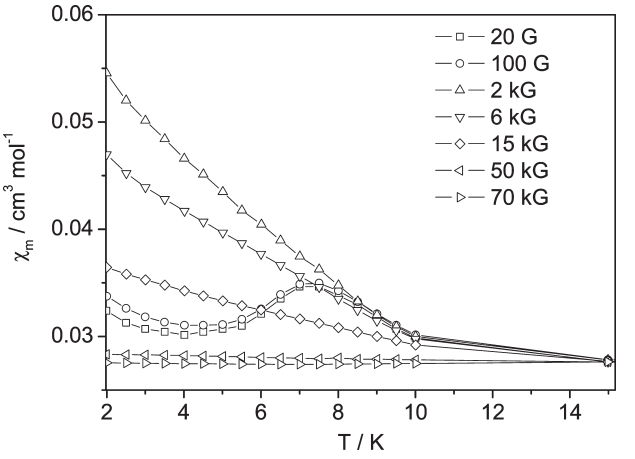

Figure 14. Plots of FC data versus T for **3** at various magnetic fields.

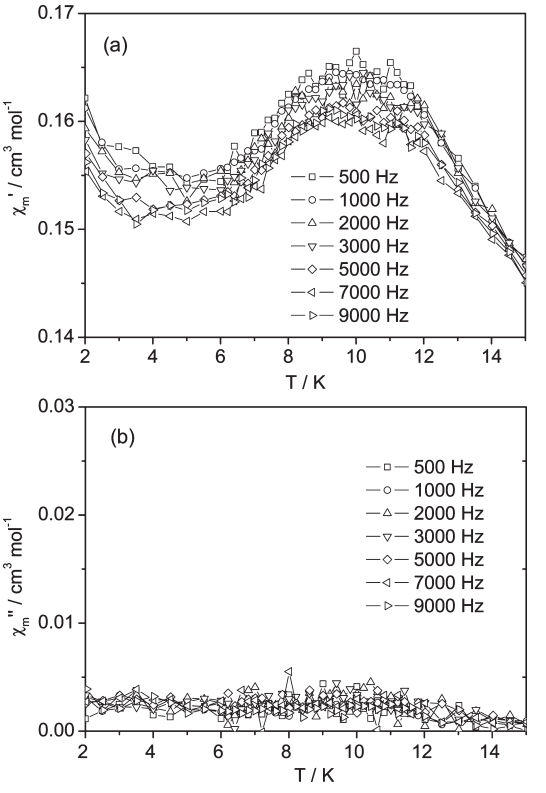

Figure 15. (a) In-phase (χ_m') and (b) out-of-phase (χ_m'') components for **3** with increasing frequencies.

(particle shape and size) should also be taken into account because in some cases the interlayer separation only could not account for the coercivity.[27] In the case of **3**, the shortest interchain distance (7.072 Å) may magnetically engender a quasi-2D lattice and the other separation (12.626 Å) may act as an interplanar spacing. With a larger interplanar distance of **3** than those of **1** and **2**, it is impossible to address the larger H_{cr} of **3** based on the situation applied to the cobalt(II) azide layered systems. Therefore, all of the structural and relevant factors should be combined to justify the hysteresis trait.

The critical fields (H_C) are obtained from the peaks of the dM/dH curves (Figure S15 in the Supporting Information).

dx.doi.org/10.1021/ic2013232 |*Inorg. Chem.* 2011, 50, 10777–10785

H_C at 2 K is 8 kG, at which a field-induced metamagnetic transition transpires. When the temperature is elevated, H_C is prone to dwindle to ca. 1.6 kG at T = 4 and 7 K and finally pass away at T = 15 K. The magnetic conversion is ascertained by the FC plots at several magnetic fields (Figure 14). The maximum at $T_{max} \approx 7.5$ K in the FC plot is retained up to H = 100 G and disappears above H = 2 kG. The peak feature designates that an antiferromagnetic state is stabilized in that field. The antiferromagnetic phase may be established because of the $\pi-\pi$ contacts. The critical field is estimated at $H \approx 1.6$ kG in the vicinity of T_{max}, and above that field, a weak ferromagnetic phase results. The ac data disclose that the broad peak in χ_m' is centered at $T_N \approx 10$ K without any χ_m'' responses, suggesting the existence of long-range antiferromagnetic order with a hidden spin canting (Figure 15). The $H-T$ phase diagram is shown in Figure S16 in the Supporting Information.

CONCLUSIONS

We have prepared three 1D Mn(III) coordination polymers with the Schiff bases (L1 for **1**, L2 for **2**, and L3 for **3**) bridged by end-to-end azides. The crystal systems and structural parameters are altered by relying on the Schiff bases used. The variable-temperature magnetic measurements reveal that intrachain antiferromagnetic couplings operate between the magnetic centers via azide bridges, and spin-canting behavior is obvious at low temperatures. Interestingly, the field-induced metamagnetic transition from an antiferromagnetic state to a weak ferromagnetic phase takes place in **1** and **3**, whereas the field-induced two-step magnetic phase transition occurs in **2**. The exchange coupling constant (J) of **2** is larger than those of **1** and **3**, which is likely relevant to the Mn$-$N$_{ax}$ bond lengths. Notably, a significantly high T_c of 38 K is observed in **2**, which is compared with critical temperatures of 11 K for **1** and 10 K for **3**. In addition, **3** exhibits the highest coercive field (2.8 kG) among azide-bridged Mn^{III} systems examined so far. The long-range order can be understood in terms of the combined contributions of the intrachain exchange couplings (J) and through-space dipolar interaction between the neighboring chains. The finding of such a high ordering temperature (38 K) in the spin-canted 1D chain system (**2**) without hydrogen-bonding and/or $\pi-\pi$ contacts between the chain structures is surprising, which may provide a strategy to developing high-T_c molecular magnets by manipulating the dipolar interactions.

ASSOCIATED CONTENT

Supporting Information. X-ray crystallographic files in CIF format and additional structural and magnetic data for the complexes. This material is available free of charge via the Internet at http://pubs.acs.org.

AUTHOR INFORMATION

Corresponding Author
*E-mail: cshong@korea.ac.kr.

ACKNOWLEDGMENT

This work was supported by grants from the National Research Foundation of Korea funded by the Korean Government (Grant 2011-0003264) and by the Priority Research Centers Program through the National Research Foundation of Korea (NRF) funded by the Ministry of Education, Science and Technology (NRF20110018396).

REFERENCES

(1) Das, A.; Gieb, K.; Krupskaya, Y.; Demeshko, S.; Dechert, S.; Klingeler, R.; Kataev, V.; Buchner, B.; Muller, P.; Meyer, F. *J. Am. Chem. Soc.* **2011**, *133*, 3433–3443.
(2) Hewitt, I. J.; Tang, J.; Madhu, N. T.; Anson, C. E.; Lan, Y.; Luzon, J.; Etienne, M.; Sessoli, R.; Powell, A. K. *Angew. Chem., Int. Ed.* **2010**, *49*, 6352–6356.
(3) Jiang, S. D.; Wang, B. W.; Su, G.; Wang, Z. M.; Gao, S. *Angew. Chem., Int. Ed.* **2010**, *49*, 7448–7451.
(4) Rinck, J.; Novitchi, G.; Van den Heuvel, W.; Ungur, L.; Lan, Y. H.; Wernsdorfer, W.; Anson, C. E.; Chibotaru, L. F.; Powell, A. K. *Angew. Chem., Int. Ed.* **2010**, *49*, 7583–7587.
(5) Gatteschi, D.; Sessoli, R. *Angew. Chem., Int. Ed.* **2003**, *42*, 268–297.
(6) Bogani, L.; Vindigni, A.; Sessoli, R.; Gatteschi, D. *J. Mater. Chem.* **2008**, *18*, 4750–4758.
(7) Harris, T. D.; Bennett, M. V.; Clerac, R.; Long, J. R. *J. Am. Chem. Soc.* **2010**, *132*, 3980–3988.
(8) Sun, H.-L.; Wang, Z.-M.; Gao, S. *Coord. Chem. Rev.* **2010**, *254*, 1081–1100.
(9) Davies, J. E.; Gatehouse, B. M.; Murray, K. S. *J. Chem. Soc., Dalton Trans.* **1973**, 2523–1973.
(10) Kennedy, B. J.; Murray, K. S. *Inorg. Chem.* **1985**, *24*, 1552–1557.
(11) Sun, H.-L.; Wang, Z.-M.; Gao, S. *Inorg. Chem.* **2005**, *44*, 2169–2176.
(12) Price, D. J.; Batten, S. R.; Moubaraki, B.; Murray, K. S. *Polyhedron* **2003**, *22*, 2161–2167.
(13) Adhikary, C.; Koner, S. *Coord. Chem. Rev.* **2010**, *254*, 2933–2958.
(14) Hong, C. S.; Do, Y. *Angew. Chem., Int. Ed.* **1999**, *38*, 193–195.
(15) Hong, C. S.; Koo, J. E.; Son, S. K.; Lee, Y. S.; Kim, Y. S.; Do, Y. *Chem.—Eur. J.* **2001**, *7*, 4243–4252.
(16) Yoo, H. S.; Kim, J. I.; Yang, N.; Koh, E. K.; Park, J. G.; Hong, C. S. *Inorg. Chem.* **2007**, *46*, 9054–9056.
(17) Nayak, S.; Evangelisti, M.; Powell, A. K.; Reedijk, J. *Chem.—Eur. J.* **2010**, *16*, 12865–12872.
(18) Li, R.-Y.; Wang, Z.-M.; Gao, S. *CrystEngComm* **2009**, *11*, 2096.
(19) Wang, X.-Y.; Wang, Z.-M.; Gao, S. *Chem. Commun.* **2008**, 281–294.
(20) Liu, X. T.; Wang, X. Y.; Zhang, W. X.; Cui, P.; Gao, S. *Adv. Mater.* **2006**, *18*, 2852–2856.
(21) Wang, X.-Y.; Wang, L.; Wang, Z.-M.; Su, G.; Gao, S. *Chem. Mater.* **2005**, *17*, 6369–6380.
(22) Reddy, K. R.; Rajasekharan, M. V.; Tuchagues, J. P. *Inorg. Chem.* **1998**, *37*, 5978–5982.
(23) Monfort, M.; Ribas, J.; Solans, X.; Font-Bardí, M. *Inorg. Chem.* **1996**, *35*, 7633–7638.
(24) Yin, P.; Gao, S.; Zheng, L.-M.; Wang, Z.; Xin, X.-Q. *Chem. Commun.* **2003**, 1076–1077.
(25) Wang, X.-Y.; Wang, L.; Wang, Z.-M.; Gao, S. *J. Am. Chem. Soc.* **2006**, *128*, 674–675.
(26) Jia, Q.-X.; Tian, H.; Zhang, J.-Y.; Gao, E.-Q. *Chem.—Eur. J.* **2011**, *17*, 1040–1051.
(27) Gao, E.-Q.; Liu, P.-P.; Wang, Y.-Q.; Yue, Q.; Wang, Q.-L. *Chem.—Eur. J.* **2009**, *15*, 1217–1226.
(28) Liu, T.-F.; Fu, D.; Gao, S.; Zhang, Y.-Z.; Sun, H.-L.; Su, G.; Liu, Y.-J. *J. Am. Chem. Soc.* **2003**, *125*, 13976–13977.
(29) Miyasaka, H.; Saitoh, A.; Abe, S. *Coord. Chem. Rev.* **2007**, *251*, 2622–2664.
(30) Ge, C.-H.; Cui, A.-L.; Ni, Z.-H.; Jiang, Y.-B.; Zhang, L.-F.; Ribas, J.; Kou, H.-Z. *Inorg. Chem.* **2006**, *45*, 4883–4885.
(31) Ko, H. H.; Lim, J. H.; Kim, H. C.; Hong, C. S. *Inorg. Chem.* **2006**, *45*, 8847–8849.
(32) Liu, C. M.; Zhang, D. Q.; Zhu, D. B. *Inorg. Chem.* **2009**, *48*, 4980–4987.
(33) Saha, S.; Mal, D.; Koner, S.; Bhattacherjee, A.; Gütlich, P.; Mondal, S.; Mukherjee, M.; Okamoto, K.-I. *Polyhedron* **2004**, *23*, 1811–1817.

(34) Stamatatos, T. C.; Christou, G. *Inorg. Chem.* **2009**, *48*, 3308–3322.
(35) Viciano-Chumillas, M.; Tanase, S.; Mutikainen, I.; Turpeinen, U.; de Jongh, L. J.; Reedijk, J. *Inorg. Chem.* **2008**, *47*, 5919–5929.
(36) Yoon, J. H.; Lee, J. W.; Ryu, D. W.; Yoon, S. W.; Suh, B. J.; Kim, H. C.; Hong, C. S. *Chem.—Eur. J.* **2011**, *17*, 3028–3034.
(37) Yoon, J. H.; Ryu, D. W.; Kim, H. C.; Yoon, S. W.; Suh, B. J.; Hong, C. S. *Chem.—Eur. J.* **2009**, *15*, 3661–3665.
(38) Yuan, M.; Zhao, F.; Zhang, W.; Wang, Z.-M.; Gao, S. *Inorg. Chem.* **2007**, *46*, 11235–11242.
(39) Lu, Z.; Yuan, M.; Pan, F.; Gao, S.; Zhang, D.; Zhu, D. *Inorg. Chem.* **2006**, *45*, 3538–3548.
(40) Tabellion, F. M.; Seidel, S. R.; Arif, A. M.; Stang, P. J. *Angew. Chem., Int. Ed.* **2001**, *40*, 1529–1532.
(41) Yoo, H. S.; Ko, H. H.; Ryu, D. W.; Lee, J. W.; Yoon, J. H.; Lee, W. R.; Kim, H. C.; Koh, E. K.; Hong, C. S. *Inorg. Chem.* **2009**, *48*, 5617–5619.
(42) Dzyaloshinsky, I. *J. Phys. Chem. Solids* **1958**, *4*, 241–255.
(43) Moriya, T. *Phys. Rev.* **1960**, *120*, 91–98.
(44) Abu-Youssef, M. A. M.; Mautner, F. A.; Vicente, R. *Inorg. Chem.* **2007**, *46*, 4654–4659.
(45) Bellitto, C.; Bauer, E. M.; Ibrahim, S. A.; Mahmoud, M. R.; Righini, G. *Chem.—Eur. J.* **2003**, *9*, 1324–1331.
(46) Cao, D.-K.; Li, Y.-Z.; Zheng, L.-M. *Inorg. Chem.* **2007**, *46*, 7571–7578.
(47) Fisher, M. E. *Am. J. Phys.* **1964**, *32*, 343–346.
(48) Manson, J. L.; Kmety, C. R.; Palacio, F.; Epstein, A. J.; Miller, J. S. *Chem. Mater.* **2001**, *13*, 1068–1073.
(49) Jia, H.-P.; Li, W.; Ju, Z.-F.; Zhang, J. *Chem. Commun.* **2008**, 371–373.
(50) Wang, X.-Y.; Wei, H.-Y.; Wang, Z.-M.; Chen, Z.-D.; Gao, S. *Inorg. Chem.* **2005**, *44*, 572–583.
(51) Yin, P.; Gao, S.; Zheng, L.-M.; Wang, Z.; Xin, X.-Q. *Chem. Commun.* **2003**, 1076–1077.
(52) Coronado, E.; Delhaes, P.; Gatteschi, D.; Miller, J. S. *Magnetic Phenomena in Molecular Materials*; Kluwer Academic Publishers: Dordrecht, The Netherlands, 1996.
(53) Coronado, E.; Gomez-Garcia, C. J.; Nuez, A.; Romero, F. M.; Waerenborgh, J. C. *Chem. Mater.* **2006**, *18*, 2670–2681.
(54) Drillon, M.; Panissod, P. *J. Magn. Magn. Mater.* **1998**, *188*, 93–99.
(55) Fujita, W.; Awaga, K. *Inorg. Chem.* **1996**, *35*, 1915–1917.
(56) Rabu, P.; Rouba, S.; Laget, V.; Hornick, C.; Drillon, M. *Chem. Commun.* **1996**, 1107–1108.